Research Article | Vol. 28, No. 4 / 17 February 2020 / Optics Express 4786
Optics EXPRESS

Design and simulation of losses in Ge/SiGe terahertz quantum cascade laser waveguides

K. Gallacher,[1] M. Ortolani,[2] K. Rew,[1] C. Ciano,[3] L. Baldassarre,[2] M. Virgilio,[4] G. Scalari,[5] J. Faist,[5] L. Di Gaspare,[3] M. De Seta,[3] G. Capellini,[3,6] T. Grange,[7] S. Birner,[7] and D. J. Paul[1,*]

[1]*University of Glasgow, James Watt School of Engineering, Rankine Building, Oakfield Avenue, Glasgow G12 8LT, UK*
[2]*Dipartimento di Fisica, Universita di Roma La Sapienza, Piazzale Aldo Moro 5, I-00185 Roma, Italy*
[3]*Dipartimento di Scienze, Universita di Roma Tre, Roma 00146, Italy*
[4]*Universitá di Pisa, Dipartimento di Fisica "Enrico Fermi", Largo Pontecorvo 3, I-56127 Pisa, Italy*
[5]*Institute for Quantum Electronics, ETH Zurich, Zurich 8093, Switzerland*
[6]*IHP–Leibniz-Institut für Innovative Mikroelectronik, Im Technologiepark 25, D-15236 Frankfurt (Oder), Germany*
[7]*nextnano GmbH, Lichtenbergstr. 8, Garching bei München 85748, Germany*
[*]*douglas.paul@glasgow.ac.uk*

Abstract: The waveguide losses from a range of surface plasmon and double metal waveguides for Ge/$Si_{1-x}Ge_x$ THz quantum cascade laser gain media are investigated at 4.79 THz (62.6 μm wavelength). Double metal waveguides demonstrate lower losses than surface plasmonic guiding with minimum losses for a 10 μm thick active gain region with silver metal of 21 cm^{-1} at 300 K reducing to 14.5 cm^{-1} at 10 K. Losses for silicon foundry compatible metals including Al and Cu are also provided for comparison and to provide a guide for gain requirements to enable lasers to be fabricated in commercial silicon foundries. To allow these losses to be calculated for a range of designs, the complex refractive index of a range of nominally undoped $Si_{1-x}Ge_x$ with x = 0.7, 0.8 and 0.9 and doped Ge heterolayers were extracted from Fourier transform infrared spectroscopy measurements between 0.1 and 10 THz and from 300 K down to 10 K. The results demonstrate losses comparable to similar designs of GaAs/AlGaAs quantum cascade laser plasmon waveguides indicating that a gain threshold of 15.1 cm^{-1} and 23.8 cm^{-1} are required to produce a 4.79 THz Ge/SiGe THz laser at 10 K and 300 K, respectively, for 2 mm long double metal waveguide quantum cascade lasers with facet coatings.

1. Introduction

The terahertz part of the electromagnetic spectrum (0.3 to 10 THz) has been heavily studied over the last decade [1] as a range of applications including non-destructive test [2], oncology imaging (skin [3] and breast cancer [4]), spectroscopic identification [5], security imaging [6] and THz communications [7] have driven a range of sources, detectors and passive optical components to enable useful systems. Practical and cheap high-power sources have always been difficult to achieve in the THz region with gas lasers, accelerators and vacuum electronic sources all demonstrating impressive THz output powers but are too expensive for many mass market applications [8,9]. Photo-conductive antenna, multiplied Gunn diodes and different frequency mixing systems, whilst arguably more practical, have relatively low powers compared to the levels required for some of the main and proposed applications [8,9].

#384993 https://doi.org/10.1364/OE.384993
Journal © 2020 Received 4 Dec 2019; revised 22 Jan 2020; accepted 24 Jan 2020; published 5 Feb 2020

Optics EXPRESS

There are few semiconductor materials with bandgaps comparable to THz energies. Intersubband quantum cascade laser (QCL) [10] using optical transitions inside quantum wells are ideal to produce semiconductor diode lasers at THz frequencies. QCLs were first demonstrated at THz frequencies in 2002 [11] and since then the improvement in performance has been impressive [12]. For III-V QCLs below the restrahlen band in frequency, CW sources have been demonstrated from 1.2 THz up to 4.9 THz [12] by a large number of groups and output powers above 1 W [13] have also been achieved. The addition of magnetic fields has allowed operation down to 680 GHz [14]. These results whilst impressive, however, are predominantly at cryogenic temperatures and the output powers decrease as the operating temperature is raised. Recently pulsed operation on a Peltier cooler at 210 K has been demonstrated with output powers of 1.2 mW [15] which requires comparison with the 40 K output power of 200 mW.

A key problem for high temperature operation of THz QCLs with III-V materials is the thermally activated relaxation mechanisms between the upper and lower radiative states for the laser resulting from polar optical phonon scattering through the Frölich interaction [12]. At low temperatures, below the LO-phonon energy (36 meV in GaAs), this scattering is suppressed but as the temperature rises the upper state lifetime is reduced as the polar optical phonon scattering increases which results in a significant reduction in the gain of the laser. By a specific temperature, the gain has reduced sufficiently that lasing is then not possible. This is a fundamental material issue limiting the high temperature performance and preventing room temperature operation of III-V THz QCLs.

Group IV materials are fundamentally different to III-V materials in that the non-polar crystal results in no Frölich interaction and so there is no polar optical phonon scattering mechanism available to degrade the upper state lifetimes as the temperature is raised. Instead the electron-phonon interaction is through deformation potential scattering which has a smaller dependence on temperature compared to polar-optical phonon scattering. This has been demonstrated in many experimental measurements of vertical intersubband transitions inside p-type SiGe quantum wells [16–18], diagonal transitions between subbands in adjacent p-type SiGe quantum wells [19] and in n-type Ge quantum wells [20,21]. All these experiments demonstrate long intersubband lifetimes, compared to GaAs/AlGaAs quantum wells, with relatively weak temperature dependence at least up to room temperature.

The first THz electroluminescence from SiGe/Si intersubband devices was from p-type quantum wells [22] where THz impurity transition electroluminescence was also observed [23]. The first quantum cascade emitters demonstrated electroluminescence from vertical [24] then diagonal intersubband transitions [25] in staircase structures but these devices were limited by domain formation. Phonon depopulation [26] and especially bound-to-continuum designs [27] produced the best gain but the intermixing of p-type subbands and the relatively large effective masses severely restrict the gain in p-type QCL designs to well below the waveguide losses. n-type Ge quantum wells were suggested for higher gain QCL devices [28] but the segregation of n-type doping in $Si_{1-x}Ge_x$ heterolayers restricted experimental research in this area until recently. Narrow absorption linewidths from $Ge/Si_{1-x}Ge_x$ quantum wells [29,30] and optical pumped n-type coupled $Ge/Si_{1-x}Ge_x$ quantum wells [21,31] have been demonstrated but to date no electrically pumped structures. Modelling of $Ge/Si_{1-x}Ge_x$ QCL structures suggest that gain of at least 20 cm^{-1} can be obtained at room temperature increasing to 65 cm^{-1} at 30 K with suitably designed active layers [32]. Previously it was shown that bound-to-continuum designs may have up to 90 cm^{-1} of gain at 4 K [33]. Whilst waveguide losses have been simulated for $Si/Si_{1-x}Ge_x$ with $x<0.4$ [34,35], to date there has been little modelling of the losses in $Ge/Si_{1-x}Ge_x$ THz waveguides with far higher Ge contents as required for n-type QCLs where refractive indexes are higher [36]. The electron transport in Ge quantum wells is in the L-valley rather than Δ-valley states in the conduction band resulting in higher mobility and lower effective masses compared to the Si rich materials.

Optics EXPRESS

In this work, the waveguide losses from average content $Si_{0.1}Ge_{0.9}$ QCL active regions are calculated for a range of single plasmon and double metal waveguide designs at THz frequencies. Fourier Transform InfraRed (FTIR) spectroscopy was used to measure a range of doped and nominally-undoped $Si_{1-x}Ge_x$ heterostructures with x = 0.7 to 1.0 to allow the real and imaginary parts of the refractive index ($n + ik$) to be obtained between 1 and 10 THz and used as the input data for the simulations. The effects of free carrier absorption on the waveguide loss will be investigated by varying the thickness of doped n-Ge electrical contact regions of the waveguides used to form Ohmic contacts. The temperature dependence of the losses will be calculated as well as an estimate of the manufacturing tolerances from reduced electrical conductivity observed in thin metals films typically used to fabricate waveguides. Finally some estimates of the minimum gain required to produce a QCL in the THz using $Ge/Si_{1-x}Ge_x$ heterostructures as a function of temperature will be derived.

2. Material choice and THz optical data

For GaAs/AlGaAs THz QCLs, most single and double metal plasmon waveguides use Au as the metal waveguide. More recently both Cu [37] and Ag [38] have been used for double metal waveguides due to their higher electrical and thermal conductivity compared to Au. A comparison of Ag, Au and Cu on GaAs/AlGaAs THz QCLs has demonstrated that Ag provides the lowest waveguide losses and lowest lasing thresholds [38]. Au is a fast diffuser and a deep level impurity in Si, Ge and SiO_2 [39–41] and therefore it is incompatible with all silicon foundries that might microfabricate $Ge/Si_{1-x}Ge_x$ QCL devices. Ag has similar deep levels but the diffusivity in Si is 3 orders of magnitude less [39], in Ge it is two orders of magnitude less [40] and in SiO_2 is one order of magnitude less than Au for similar anneal conditions [41]. Both Al and Cu are considered to be silicon foundry compatible metals although Cu requires better liners and diffusion barriers to prevent diffusion.

An additional important consideration for n-type $Ge/Si_{1-x}Ge_x$ QCLs is choosing a metal which can also form an Ohmic contact as Fermi level pinning close to the valence band edge results in an energy barrier to electrons entering the semiconductor from a metal and a significant contact resistivity [42]. NiGe alloys have demonstrated contact resistivities of 2×10^{-7} Ω-cm^2 but only for contact n-type doping of 3×10^{19} cm^{-3}. A better choice is Ag (1% Sb) which has demonstrated sufficiently low resistivity contacts even at n-Ge contact doping of 10^{18} cm^{-3} [43]. The Ag is also ideal for plasmon waveguides at THz frequencies as explained above.

The complex refractive index with real and imaginary parts ($n + ik$) can be calculated from the Drude-Lorentz theory [44]. The complex dielectric function, ε with real and imaginary parts $\varepsilon_r + i\varepsilon_i$ respectively is defined at a particular angular frequency ω (= $2\pi\nu$ where ν is the frequency) in mks units as

$$\varepsilon = \varepsilon_r + i\varepsilon_i = \varepsilon_\infty \left(1 - \frac{\omega_p^2}{\omega^2 + \frac{1}{\tau^2}}\right) - i\frac{1}{\omega\tau}\left(\frac{\varepsilon_\infty \omega_p^2}{\omega^2 + \frac{1}{\tau^2}}\right) + \sum_{i=1}^{2} \frac{c^2 S_i^2}{(\omega_i^2 - \omega^2) - i\omega\gamma_i} \tag{1}$$

where ε_∞ is the high-frequency dielectric screening constant in a material with electrical conductivity, σ with a free carrier density, N for electrons with effective mass, m^*, electric charge, q and the speed of light in a vacuum, c. Two Lorentz oscillator terms, S_i with Lorentz frequency ω_i and width, γ_i are added for the inter-valence band transitions in p-type semiconductors. For metals and heavily doped n-type semiconductors, the Lorentz S_i terms are zero and Eq. (1) reduces to the well known Drude formula. The plasma frequency, ω_p and relaxation time, τ are defined as

$$\omega_p = 2\pi\nu_p = \sqrt{\frac{Nq^2}{m^*\varepsilon_\infty\varepsilon_0}} \quad \text{and} \quad \tau = \frac{\sigma m^*}{Nq^2} \tag{2}$$

Optics EXPRESS

The real, n and imaginary, k refractive index components are obtained from Eq. (1) using

$$n = \frac{1}{\sqrt{2}}\sqrt{(\varepsilon_r^2 + \varepsilon_i^2)^{\frac{1}{2}} + \varepsilon_r} \quad \text{and} \quad k = \frac{1}{\sqrt{2}}\sqrt{(\varepsilon_r^2 + \varepsilon_i^2)^{\frac{1}{2}} - \varepsilon_r} \tag{3}$$

In this work we choose four metals to simulate the waveguide losses. First is Au to allow a direct comparison with many III-V THz QCLs [11]. Al and Cu are chosen as they are silicon foundry compatible and Ag is chosen as it provides the lowest losses in III-V THz QCLs [38] and also forms a good Ohmic contact to n-Ge [43]. The 300 K refractive index data used in the simulations for Al and Cu were taken from Ref. [45]. For Ag, the refractive index data from Ref. [46] was used and for Au the data from Ref. [47]. The real and imaginary parts of the complex refractive index, $n + ik$, between 0.06 and 10 THz are plotted in Fig. 1(a) for the four metals being considered. An analytical formula for the waveguide loss, α_{sp} from a surface plasmon waveguide is

$$\alpha_{sp} = \frac{4\pi n_{metal} k_{metal} n_{SiGe}^3}{\left[(n_{metal}^2 - k_{metal}^2)(n_{SiGe}^2 + n_{metal}^2 - k_{metal}^2)^3\right]} \frac{1}{\lambda} \approx \frac{4\pi}{\lambda} \frac{n_{metal} n_{SiGe}}{\mid k_{metal}^3 \mid} \tag{4}$$

where n_{metal} is the real part of the refractive index for the metal, k_{metal} is the imaginary part and n_{SiGe} is the real part of the semiconductor waveguide [48]. As the loss from surface plasmonic waveguides is proportional to $\frac{n}{k^3}$ for the metal plasmon guide, Ag should have the lowest losses at 300 K while Au will have the highest at 20 meV. The bulk refractive indexes used in this work suggest Ag and Cu should have similar losses. A number of experimental examples using thin metal films have demonstrated higher electrical conductivities than bulk values [38]. This effect of increased electrical conductivity for thin films will be investigated in the final section of the paper. Throughout the paper, the modal overlap, Γ is defined for the yz cross section (with light propagating down the waveguide in x) as

$$\Gamma = \frac{\int\int_{\text{active}} |E|^2 \, dydz}{\int_{-\infty}^{\infty}\int_{-\infty}^{\infty} |E|^2 \, dydz} \tag{5}$$

where the electric field is integrated over the active part of the waveguide divided by the electric field everywhere.

As the authors were unable to find any reliable refractive index data in the appropriate THz range for undoped or doped $Si_{1-x}Ge_x$ with $x \geq 0.7$, measurements were undertaken using a FTIR spectrometer. A Bruker 66vs FTIR spectrometer with a cryogenically cooled Si bolometer was used to measure a range of nominally undoped (p-type background below $\sim 5 \times 10^{15}$ cm^{-3}) $Si_{1-x}Ge_x$ (x = 0.7, 0.8 and 0.9) and doped n-Ge samples. Ge and SiGe heterostructure films of thickness varying from 400 nm to 2000 nm were grown by chemical vapor deposition on float zone Si (001) wafers [49]. Square dies of 1×1 cm^2 were cut from the wafers, mounted in a transmission/reflection sample holder and measured by FTIR spectroscopy. The reflectance and transmittance spectra are separately acquired in two different optical beam path configurations, but the sample has not been unmounted between the two measurements. 512 scans at a resolution of 4 cm^{-1} in rapid-scan mode were acquired for each sample. The Drude-Lorentz model was employed to reproduce the refractive index value, the free carrier absorption and the inter-valence band transition (present only in the case of p-type samples). The substrate wafer optical constants (measured separately) are also included in the transmission/reflection model. For the p-type $Si_{1-x}Ge_x$ samples, the Lorentz frequency and width terms were assumed identical for all samples and set to the following values: $\omega_1/(2\pi)$ = 43.9 THz, γ_1 = 35.4 THz, $\omega_2/(2\pi)$ = 67.0 THz, γ_2 = 59.4 THz. The results with the fitted Lorentz oscillator strengths are presented in Table 1. All the complex refractive index data for the n-Ge and $Si_{1-x}Ge_x$ heterolayers are available to download from a data archive.

Optics EXPRESS

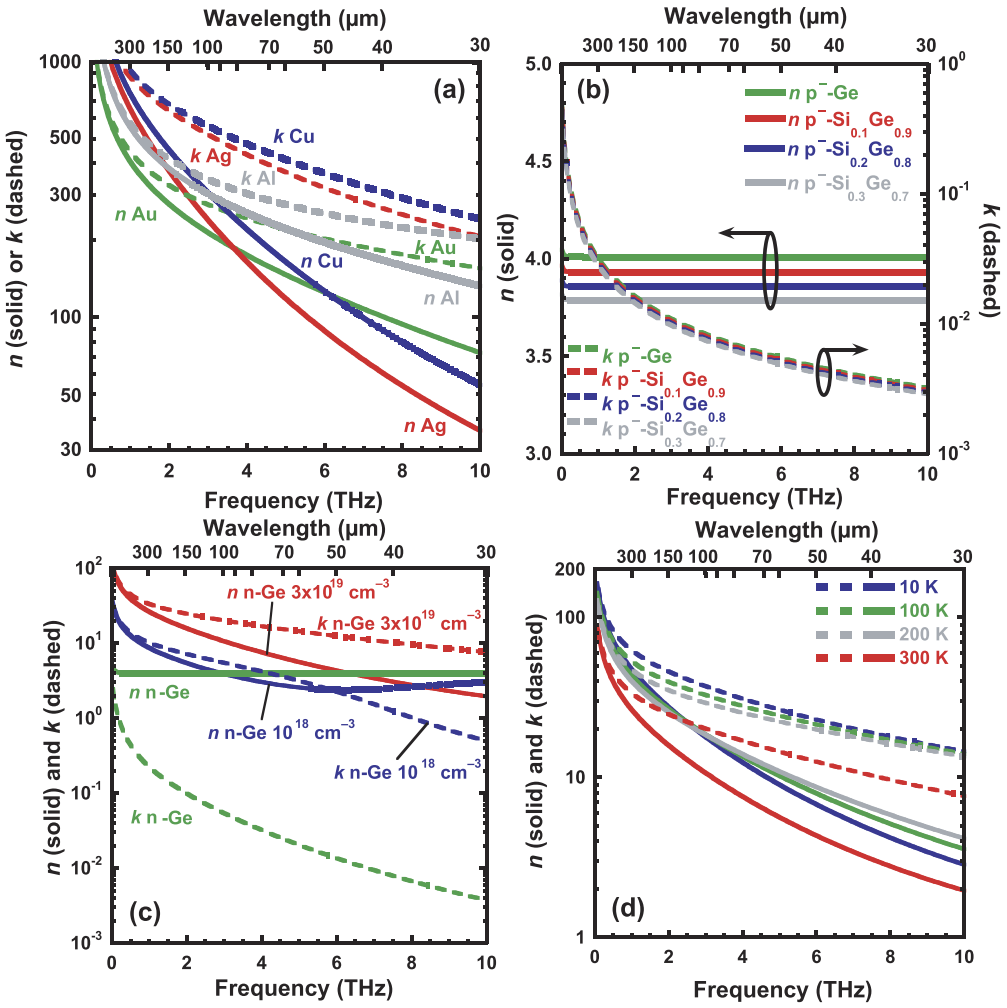

Fig. 1. (a) The $n + ik$ values of the refractive index at 300 K for a range of silicon foundry compatible and incompatible metals between 0.06 and 10 THz. (b) The measured $n + ik$ for a range of $Si_{1-x}Ge_x$ epitaxial materials with low p-type doping. (c) The measured $n + ik$ for a range of n-Ge epitaxial materials with different doping densities. (d) The measured $n + ik$ for n-Ge doped at 3×10^{19} cm^{-3} from 10 K to 300 K.

Table 1. The extracted Drude-Lorentz parameters at 300 K for SiGe materials.

sample	ν_p (THz)	τ^{-1} (THz)	ϵ_∞	S_1 (cm^{-1})	S_2 (cm^{-1})
n-Ge ($N = 3 \times 10^{19}$ cm^{-3})	37.6	7.4	16.6	0	0
n-Ge ($N = 10^{19}$ cm^{-3})	22.6	4.2	16.6	0	0
n-Ge ($N = 10^{18}$ cm^{-3})	7.3	4.2	16.1	0	0
n^--Ge ($N \sim 5 \times 10^{15}$ cm^{-3})	0.73	4.2	16.1	0	0
p^--Ge ($N \sim 5 \times 10^{15}$ cm^{-3})	0.79	4.2	16.1	97	77
p^--$Si_{0.1}Ge_{0.9}$ ($N \sim 5 \times 10^{15}$ cm^{-3})	0.76	36	15.4	94	75
p^--$Si_{0.2}Ge_{0.8}$ ($N \sim 5 \times 10^{15}$ cm^{-3})	0.75	36	14.9	91	73
p^--$Si_{0.3}Ge_{0.7}$ ($N \sim 5 \times 10^{15}$ cm^{-3})	0.74	36	14.3	89	71

Optics EXPRESS

The data are presented in Fig. 1(b) for nominally undoped $Si_{1-x}Ge_x$ (with x = 0.7, 0.8 and 0.9) and Fig. 1(c) for heavily doped n-Ge with activated P doping of 10^{17} cm^{-3}, 10^{18} cm^{-3} and 3×10^{19} cm^{-3}. The heavily doped n-Ge samples are predicted to show a strong temperature dependence of the optical constants. The n-Ge sample doped at 3×10^{19} cm^{-3} was therefore also mounted in an optical cryostat (Janis Research Corp.) installed in the same FTIR spectrometer, and the transmission and reflectance spectra were measured as a function of temperature in the 10 K to 300 K range (Fig. 1(d)). The extracted Drude parameters are presented in Table 2.

Table 2. The extracted Drude parameters for n-Ge with $N = 3 \times 10^{19}$ cm^{-3}.

temperature	ν_p (THz)	τ^{-1} (THz)	ϵ_∞
T=300 K	37.6	7.4	16.6
T=200 K	37.6	6.2	16.6
T=100 K	37.6	5.0	16.6
T=10 K	37.6	3.8	16.6

3. Waveguide modelling

For the QCL designs used in this paper, doped layers for Ohmic contacts are essential and so Eq. (4) cannot be used to calculate the losses. The waveguides were therefore simulated using a finite difference eigenmode solver (Lumerical) with metal and $Si_{1-x}Ge_x$ complex refractive indexes at 300 K unless otherwise stated. The present simulations are limited to the waveguide losses related to the metals, the contact layers and the bulk dielectric behaviour of the heterostructures and ignores any 2D resonance effects that may be observed in QCL heterostructure designs. We have chosen 20 meV or 4.79 THz (62.6 μm wavelength) as the design frequency for the active regions [32] and therefore for the waveguide modelling in this work. To achieve strain symmetrisation for n-type Ge quantum wells with $Si_{1-x}Ge_x$ barriers with Ge content, x between 0.65 to 0.85 will require an average Ge content between 0.9 to 0.95 [8]. We therefore choose $Si_{0.1}Ge_{0.9}$ for the waveguide active material throughout the paper as we have experimental data for that composition (Fig. 1(b)). Changes to the average composition between 0.9 to 0.95 have been estimated to result in less than 1% change to the losses by using Eq. (4) and a quadratic fit to estimate n_{SiGe} for x = 0.95. Two n-Ge doped layers have been added to either side of the $Si_{0.1}Ge_{0.9}$ average composition waveguide region to allow the formation of top and bottom Ohmic contacts. It should be noted that the 3D mean free path of the n-Ge with 3×10^{19} cm^{-3} is 8 nm so for all the n-Ge heterolayers used in the paper the electron transport is 3D with bulk properties rather than 2D heterolayers. These regions can contribute to free carrier loss but can also contribute as part of the surface plasmon waveguides due to being doped above the metal-insulator transition [49]. Initial simulations have demonstrated that as part of the plasmon waveguide, higher doping results in lower loss suggesting the plasmonic guide effect is dominating over the free carrier loss. Throughout the paper, the n-Ge contact regions will use activated dopant concentrations of $N_D = 3 \times 10^{19}$ cm^{-3} (Fig. 1(c)).

Figure 2 shows the calculated eigen-modes for (a) a surface plasmon and (b) a double metal waveguide with a 10 μm thick $Si_{0.1}Ge_{0.9}$ active region with 50 nm n-Ge top and bottom contact regions and 400 nm Ag top and in (b) also the bottom. The inserts to Fig. 2 show the layer stacks used throughout the paper for (a) surface plasmon and (b) double metal waveguides where the only variables will be the thickness of the active i-$Si_{0.1}Ge_{0.9}$ region (of y μm thickness) and the n-Ge contact layers (of x nm thickness). QCLs with electron to electron intersubband transitions only support z-polarized or TM modes. For Group IV QCLs, low loss to achieve lasing is much more important than single mode operation so for all the simulations a constant waveguide width of 100 μm will be used. This supports multiple modes at 4.79 THz (62.6 μm wavelength) but is

Optics EXPRESS

sufficiently wide to be able provide operation even at 1 THz (~ 300 μm wavelength). Figure 2 does indicate that waveguides of ≤ 60 μm width will support only a single TM0 mode for both surface plasmon and double metal waveguides. Measurements of mid-infrared Ge waveguides using comparable fabrication techniques to those required for the Ge/SiGe QCL waveguides indicate that losses from sidewall scattering are not the limiting factor at 10 μm wavelength for the level of sidewall roughness produced from typical fluorine based etches [50] and at longer THz wavelengths such scattering mechanisms are expected to be negligible. Therefore sidewall scattering is not expected to play any significant role in the losses for Ge/SiGe THz waveguides and therefore has not been included in the modelling.

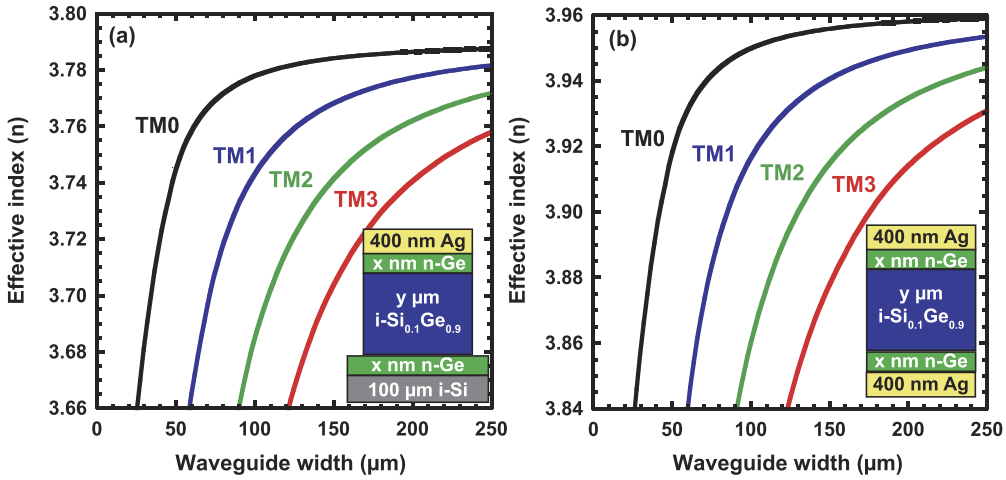

Fig. 2. The calculated effective modal indices versus the waveguide width at 4.79 THz (62.6 μm wavelength) for a 10 μm thick $Si_{0.1}Ge_{0.9}$ active region with 50 nm n-Ge top and bottom contact regions with (a) a single 400 nm Ag top metal contact as a surface plasmon waveguide and (b) an additional 400 nm Ag bottom metal contact in a double metal waveguide configuration. The inserts show (a) the surface plasmon waveguides and (b) the double metal waveguide layer stacks modelled throughout the paper.

While double metal waveguides are now recognised as producing lower losses, the first THz QCL was demonstrated with a single top metal guide forming a surface plasmonic waveguide [11] and these waveguides are far easier to fabricate. Figure 3(a) shows the simulated waveguide losses and modal overlap at 4.79 THz (62.6 μm) for surface plasmon waveguides with 50 nm n-Ge top and bottom contact layers and a 400 nm thick metal top surface plasmon waveguide for a 100 μm width as a function of the thickness of the $Si_{0.1}Ge_{0.9}$ active layer. The structure is modelled on top of a silicon substrate of thickness 100 μm. It is assumed that any bottom metal contacts are placed at a sufficient lateral distance from the ridge waveguide to prevent any additional loss. As the active region is increased in thickness, the waveguide loss decreases and the modal overlap increases. For the thinnest active regions below 6 μm, the waveguides are getting close to the point where the optical modes cannot be supported. As can be observed, Ag provides the lowest losses which is similar to GaAs/AlGaAs THz waveguides [38] whilst Cu provides the lowest losses for silicon foundry compatible fabrication.

A 50 nm n-Ge bottom contact layer provides challenges to etch stop and form Ohmic contacts for such surface plasmon waveguides. The thickness of this layer also contributes to a series resistance which can be detrimental to the electron temperature if not controlled. Thicker contacts with lower series resistance are expected to increase the waveguide loss through free carrier absorption [8] so the design is always a compromise to achieve the best overall laser performance. Figure 3(b) presents the loss of a 10 μm $Si_{0.1}Ge_{0.9}$ active layer with 400 nm of surface metal as

Optics EXPRESS

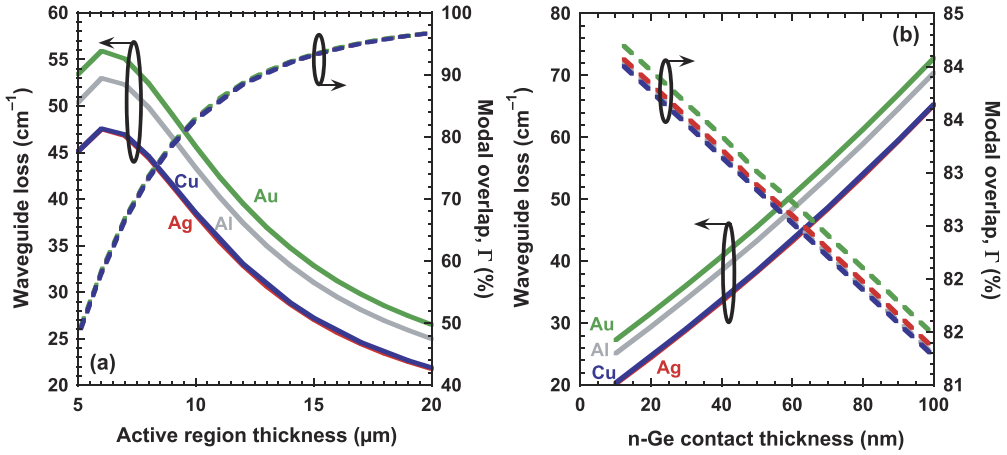

Fig. 3. (a) The waveguide losses and modal overlaps at 300 K for surface plasmon waveguides on a 100 μm wide ridge with 50 nm n-Ge top and bottom contact layers for different $Si_{0.1}Ge_{0.9}$ active region thicknesses for four different metals. (b) The waveguide losses and modal overlap for surface plasmon waveguides on a 100 μm wide ridge with a 10 μm thick $Si_{0.1}Ge_{0.9}$ active region as the n-Ge top and bottom contact regions are varied in thickness.

the top and bottom n-Ge contact layers are varied in thickness. While the losses can be reduced further when the n-Ge contact layers are reduced in thickness as the free carrier absorption reduces, the ability to etch and stop exactly on the bottom n-Ge heterolayer becomes more challenging. Figure 4 presents a cross section of the squared electric field profiles for (a) a 10 μm thick waveguide with 50 nm n-Ge contacts and (b) for a 10 μm thick waveguide with a 50 nm n-Ge top contact and a more fabrication practical 400 nm n-Ge bottom contact layer. The thicker bottom contact does improve the modal overlap but this is with the cost of a substantial increase of losses from free carrier absorption to 326 cm^{-1}. These results highlight the higher free carrier losses from doped n-Ge compared to doped n-GaAs for similar electrical conductivity due to the lower mobility and higher density of states in Ge [8].

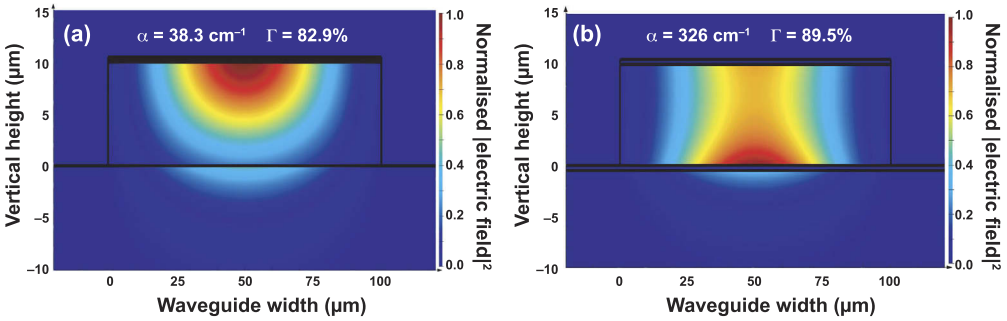

Fig. 4. (a) The normalised squared electric field at 4.79 THz (62.6 μm) in a 100 μm wide $Si_{0.1}Ge_{0.9}$ ridge with 50 nm n-Ge top and bottom contacts and a 400 nm thick Ag surface plasmon waveguide. (b) The normalised squared electric field at 4.79 THz (62.6 μm) for an identical waveguide to (a) where the bottom contact has been expanded in thickness to 400 nm of n-Ge.

In the III-V material QCL systems, double metal waveguides have demonstrated lower losses and larger modal overlap to provide lower threshold gain compared to single plasmon waveguides

Optics EXPRESS

[38]. The losses for the double metal waveguides with four different metals are demonstrated in Fig. 5(a) for 50 nm n-Ge top and bottom contacts with 400 nm metal top and bottom at 4.79 THz (62.6 μm) for different thicknesses of the $Si_{0.1}Ge_{0.9}$ active region. For all these metal systems the modal overlap has a minimum value of 99.95% and has not been included for clarity. Figure 5(b) demonstrates how the losses scale as the n-Ge contact layers are scaled. Double metal fabrication processes provide easier and more reliable methods to etch stop on the bottom contact. For the double metal process, the substrate has to be removed by etching allowing heterolayers to be grown underneath the bottom contact with sufficient changes in the refractive index to allow in-situ optical end detection inside plasma etch tools. Also series resistance effects are negligible compared to surface plasmon waveguides and are mainly related to the resistance of the n-Ge contact layers and metal to semiconductor contact resistances.

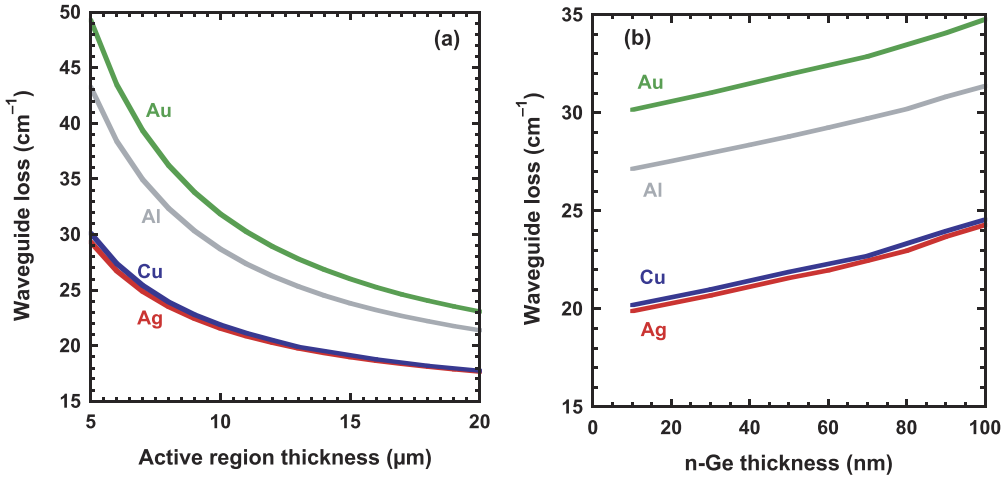

Fig. 5. (a) The waveguide losses at 300 K for double metal waveguides on a 100 μm wide $Si_{0.1}Ge_{0.9}$ ridge with 50 nm n-Ge top and bottom contact layers for different active region thicknesses for four different metals. (b) The waveguide losses for double metal plasmon waveguides with a 100 μm wide ridge and 10 μm thick $Si_{0.1}Ge_{0.9}$ active regions as the n-Ge top and bottom contact regions are varied in thickness.

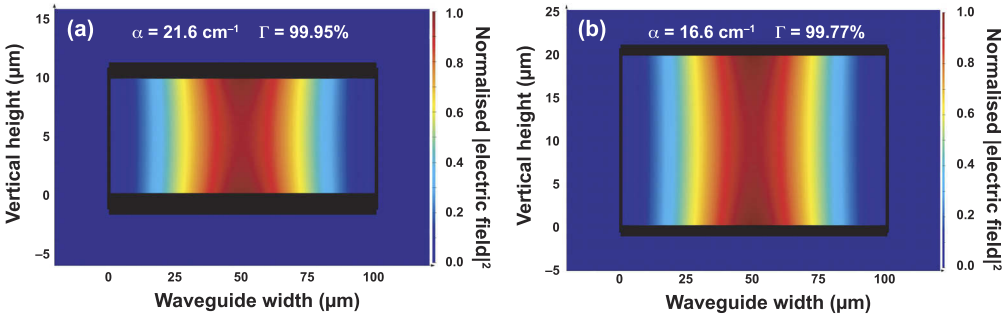

Fig. 6. (a) The normalised squared electric field at 4.79 THz (62.6 μm) in a 100 μm wide $Si_{0.1}Ge_{0.9}$ ridge of 10 μm depth with 50 nm n-Ge top and bottom contacts and a 400 nm Ag metal top and bottom double metal waveguide. (b) The normalised squared electric field at 4.79 THz (62.6 μm) in a 100 μm wide $Si_{0.1}Ge_{0.9}$ ridge of 20 μm depth with 10 nm n-Ge top and bottom contacts and a 400 nm Ag metal top and bottom double metal waveguide.

Optics EXPRESS

The squared electric field optical mode profiles are presented in Fig. 6 for double metal waveguides using 400 nm Ag. Figure 6(a) presents an easier fabrication process with larger tolerances in the contacts using 50 nm thick n-Ge contact layers and a 10 μm $Si_{0.1}Ge_{0.9}$ active region. Here the waveguide loss is 21.6 cm^{-1} for a modal overlap of 99.95% which is comparable to results from 10 μm thick GaAs/AlGaAs double metal waveguides with Ag at 3.1 THz and 300 K of ~20 cm^{-1} [38]. This suggests that the higher losses from the lower mobility in Ge compared to GaAs has significantly less impact on the losses in double metal waveguides compared to surface plasmon waveguides. Figure 6(b) takes a much more aggressive design aimed at minimising the loss at 300 K with 10 nm thick n-Ge contact layers and a 20 μm $Si_{0.1}Ge_{0.9}$ active region resulting in losses reduced to 16.6 cm^{-1} for a modal overlap of 99.95%.

4. Waveguide performance versus frequency

It is useful to understand how tolerant the waveguide losses are to changes to the emission frequency to understand how the gain of the active region must be engineered for lasers operating at different frequencies. Figure 7(a) shows the losses and modal overlaps for surface plasmon waveguides with a 10 μm active region as a function of emission frequency. At the lowest frequency (longest wavelength), below about 3.5 THz, the number of supported modes in the waveguides is reduced to a single mode and eventually a frequency is reached where the waveguides cannot guide light and the optical modes leak completely into the Si substrate. As both the waveguide losses increase and the modal overlap decrease as the frequency is reduced, the threshold gain for a laser is increasing significantly. At higher frequencies, the losses reduce and the modal overlap increases as the propagation wavelength divided by the effective refractive index of the waveguide becomes comparable to the active region thickness around 8 THz. While Eq. (4) suggests lower losses should be achieved at longer wavelength, the lower losses at shorter wavelength suggest that the reduction in the real part of the metal refractive index is the dominating factor (Fig. 1(a)).

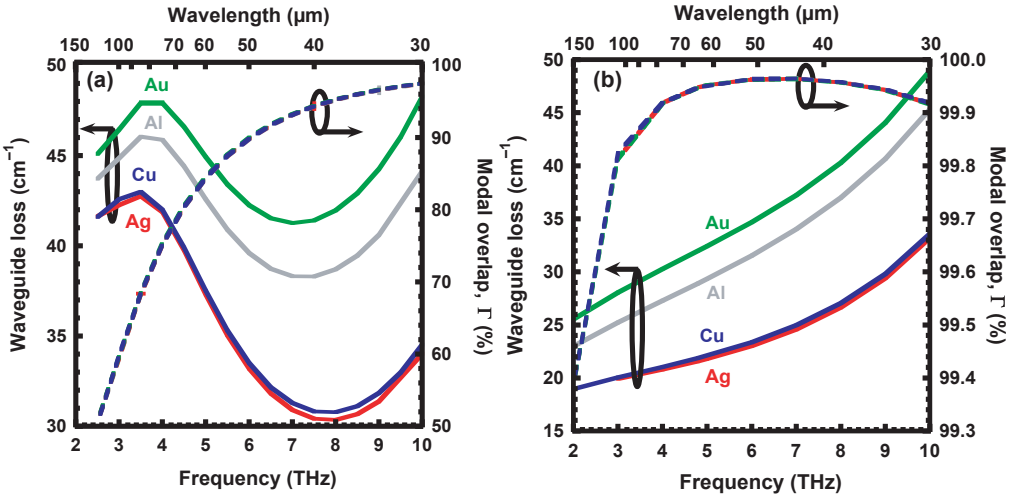

Fig. 7. (a) The waveguide losses and modal overlaps at 300 K for surface plasmon waveguides on a 100 μm wide ridge with 50 nm n-Ge top and bottom contact layers for 10 μm thick active region thicknesses for four different metals as a function of frequency. (b) The waveguide losses and modal overlaps at 300 K for double metal waveguides on a 100 μm wide ridge with 50 nm n-Ge top and bottom contact layers for 10 μm thick active region thicknesses for four different metals as a function of frequency.

Optics EXPRESS

For the double metal waveguides an opposite trend to the surface plasmon waveguides is observed (Fig. 7(b)). A slow increase in the waveguide losses is observed as the frequency is increased. It can be observed that the relative change in loss with frequency is lower for higher electrical conductivity materials. At the longer wavelengths, the Ag waveguide cannot support optical modes below about 3 THz whilst for the other metals this is reached at around 2 THz. The modal overlap decreases as the waveguide approaches the point where it stops propagating the optical modes but this decrease is less than a 1% change. The key issue for producing QCLs is that for double metal waveguides with the lowest losses using Ag, the waveguide losses only change by 3.1 cm^{-1} between 3 and 6 THz providing a large, broadband window for emission wavelength.

5. Waveguide performance and threshold gain requirements versus temperature

The focus of the paper to this point has been about waveguide losses at 300 K. Here the waveguide losses and threshold gain are investigated as a function of temperature. In addition, it is well known that the electrical conductivity of thin metal films even of a few 100 nm thickness can be significantly reduced compared to bulk metals due to additional electron scattering at grain boundaries and at rough surfaces [38,51]. Therefore in this section the waveguide losses will also be studied as a function of the optical parameters of different silver films with a range of thicknesses and compared to bulk values.

The material references used up to this point were only for room temperature parameters. FTIR was also used to extract the refractive indexes of n-Ge ($N_D = 3 \times 10^{19}$ cm^{-3}) at 10 K, 100 K and 200 K. The temperature dependence of the electrical conductivity of the metals for bulk Ag, Au and Cu were taken from Ref. [52]. Data for 170 nm and 780 nm thick Ag films was taken from Ref. [51] and 10 nm Ti with 200 nm Ag films from Ref. [38]. For Al the data was taken from Ref. [53]. The electrical conductivity for all materials are plotted in Fig. 8(a). Whilst bulk Ag has the highest 300 K electrical conductivity, Al is known to have an anomalously high electrical conductivity at low temperatures before reaching a superconducting transition point at 1.14 K [54] and this is clearly observed. Equations (1) to (3) were used to calculate the real and imaginary components of the refractive index and these are presented in Fig. 8(b).

The waveguide losses and modal overlaps were calculated at 10, 100, 200 and 300 K using the data from Figs. 8(a) and (b) for double metal waveguides with 10 μm $Si_{0.1}Ge_{0.9}$ active region, 50 nm n-Ge top and bottom contact layers and 400 nm of metal. The results were calculated at 4.79 THz (62.6 μm) for 100 μm wide waveguides as a function of temperature. Despite using metal data from different references compared to the simulations in Fig. 5, the bulk Ag and Al double metal waveguide results in Fig. 8(c) agree to within 0.2 cm^{-1}. Au has been left out for clarity to allow the variation in Ag film thickness to be clearly demonstrated. An interesting effect is that the Al anomalous electrical conductivity [54] results in lower waveguide losses than bulk Ag at the lowest temperatures. For the silicon foundry compatible metals, Al provides the lowest waveguide losses at the lowest temperatures ($\leq$ 40 K) whilst Cu provides lower losses above this temperature and is therefore the best silicon foundry compatible metal for plasmon waveguides at practical operating temperatures. It should be noted that only the results at the four temperatures have been plotted in Figs. 8(c) and (d) where experimental data was available for the $Si_{0.1}Ge_{0.9}$ and n-Ge materials as a function of temperature and no extrapolations have been used for temperatures between these data points.

The other clear effect is the electrical quality of the Ag films. A spread in loss can be observed at any fixed temperature of < 2 cm^{-1} with thinner films and those of mixed metals which have the lower electrical conductivities (Fig. 8(a)) providing the higher waveguide loss. While bulk film properties may be difficult to achieve in all laboratories, the results do indicate how much loss could be saved if an optimum metal thickness and film deposition process can be achieved

Optics EXPRESS

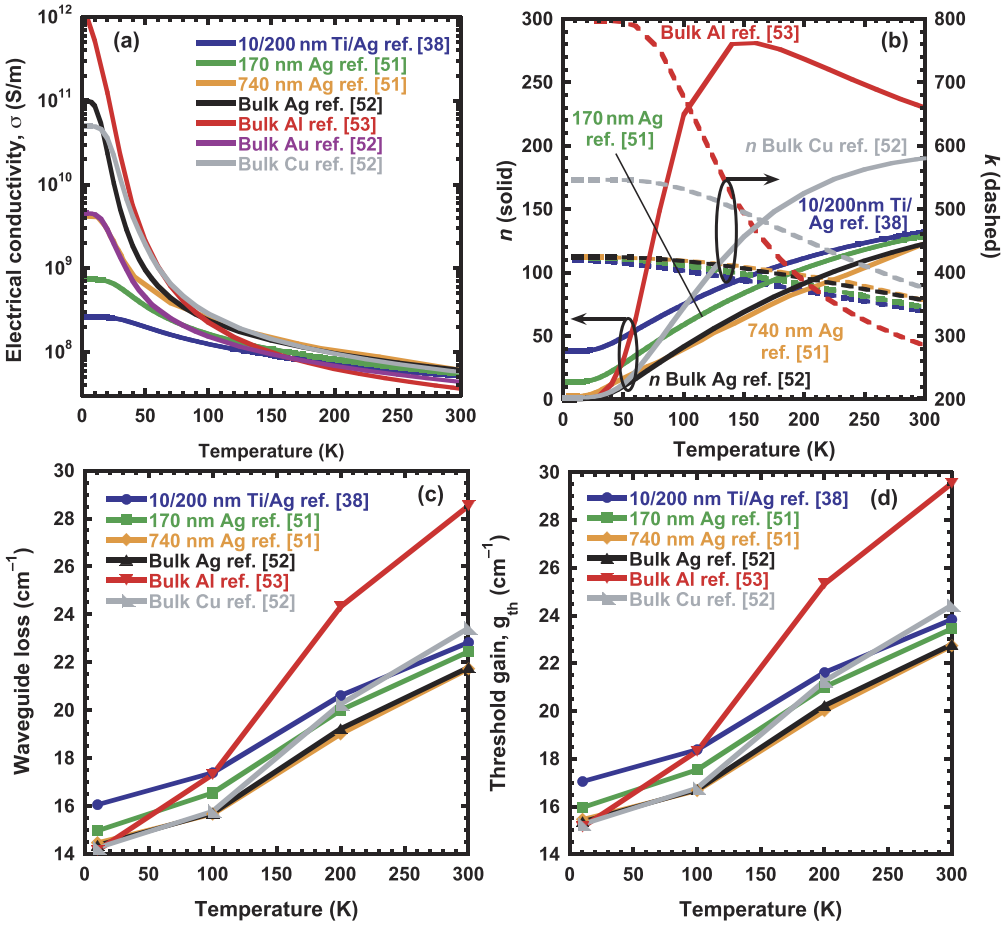

Fig. 8. (a) The temperature dependence of the electrical conductivity for the data used in the simulations. (b) The real (n) and imaginary (k) parts of the refractive index calculated from the Drude theory from the electrical conductivity in (a). The waveguide losses (c) and gain threshold (d) as a function of temperature for double metal waveguides with 10 μm $Si_{0.1}Ge_{0.9}$ active region, 50 nm n-Ge top and bottom contact layers and 400 nm of metal at 4.79 THz (62.6 μm).

for fabricating the waveguides. This variance in waveguide loss also serves to suggest that the uncertainty in the waveguide loss simulations are of order of ± 1 cm^{-1} mainly resulting from any uncertainty in the refractive index data.

The waveguide losses are not the sole loss that is required to be overcome by the gain medium to be able to achieve an operating laser. Mirror losses, α_m as well as the modal overlap must also be included in the calculation. Therefore the threshold gain, g_{th} which is the gain required for the threshold of lasing to be achieved, is calculated using

$$g_{th} = \frac{\alpha_m + \alpha_w}{\Gamma} \quad \text{where} \quad \alpha_m = \frac{1}{2L} \ln(R_1 R_2) \tag{6}$$

The mirror loss requires the waveguide length, L and also the reflectivity at each facet at the ends of the waveguides, R_1 and R_2. Longer waveguides therefore have lower mirror loss but this cannot be increased indefinitely. To provide a direct comparison with GaAs/AlGaAs THz QCLs at 3.1 THz [38], we chose a length of 2 mm and facet reflectivities of 0.82. Figure 8(d)

Optics EXPRESS

demonstrates the threshold gain required for lasing for the different Ag films and bulk Al double metal waveguides. The double metal waveguides using Al provide the lowest gain threshold of 15.1 cm^{-1} at 10 K whilst bulk Ag films produce a gain threshold of 23.8 cm^{-1} at 300 K. Figure 8(d) also indicates that metals which are too thin to achieve bulk electrical conductivities or are contaminated so that the electrical conductivity is reduced will result in higher thresholds.

6. Conclusion

The waveguide losses, modal overlaps and threshold gain have been calculated for a range of Ge/SiGe surface plasmon and double metal waveguides. FTIR was used to extract the complex refractive indexes for undoped $Si_{1-x}Ge_x$ (x = 0.7, 0.8 and 0.9) and heavily doped n-Ge which were used in the simulations. Waveguide losses were lowest for the highest doping available for the n-Ge contact regions. Double metal waveguides using Ag and Al demonstrate the lowest thresholds for lasing of 23.8 cm^{-1} at 300 K and 15.1 cm^{-1} at 10 K respectively for 2 mm long lasers with 10 μm of active region at 4.79 THz (62.6 μm). Cu provides the lowest losses for a silicon foundry compatible metal above $\sim$ 40 K for operation at practical temperatures. At the lowest temperatures (below $\sim$ 40K) Al has lower losses and threshold gain than Ag and Cu due to the anomalous electrical conductivity. The calculated double metal waveguide losses at 4.79 THz (62.6 μm) using Ge/SiGe material are comparable to GaAs/AlGaAs of similar active region thickness, length and reflectivity at 3.1 THz. The results provide a guide for the amount of gain required to achieve lasing using Ge/SiGe QCL designs. Comparing these values to the gain simulations from Ge/SiGe active regions at the same frequency [32] with 20 cm^{-1} gain at 300 K and 65 cm^{-1} at 30 K indicate that lasing should be feasible up to about 280 K if such gain and waveguide losses can be achieved experimentally.

Funding

European Union's Horizon 2020 research and innovation programme (766719); Engineering and Physical Sciences Research Council (EP/N003225/1).

Disclosures

The authors declare no conflicts of interest.

Data availability

The data associated with this work can be downloaded from the University of Glasgow data archive at https://doi.org/10.5525/gla.researchdata.950.

References

1. M. Perenzoni and D. J. Paul, eds. *Physics and Applications of Terahertz Radiation*, no. 173 in Springer Series in Optical Science (Springer, 2014).
2. J. A. Zeitler, P. F. Taday, D. A. Newnham, M. Pepper, K. C. Gordon, and T. Rades, "Terahertz pulsed spectroscopy and imaging in the pharmaceutical setting - a review," J. Pharm. Pharmacol. **59**(2), 209–223 (2007).
3. R. M. Woodward, B. E. Cole, V. P. Wallace, R. J. Pye, D. D. Arnone, E. H. Linfield, and M. Pepper, "Terahertz pulse imaging in reflection geometry of human skin cancer and skin tissue," Phys. Med. Biol. **47**(21), 3853–3863 (2002).
4. P. C. Ashworth, E. Pickwell-MacPherson, E. Provenzano, S. E. Pinder, A. D. Purushotham, M. Pepper, and V. P. Wallace, "Terahertz pulsed spectroscopy of freshly excised human breast cancer," Opt. Express **17**(15), 12444–12454 (2009).
5. P. Taday, I. Bradley, D. Arnone, and M. Pepper, "Using terahertz pulse spectroscopy to study the crystalline structure of a drug: A case study of the polymorphs of ranitidine hydrochloride," J. Pharm. Sci. **92**(4), 831–838 (2003).
6. R. Appleby and H. B. Wallace, "Standoff detection of weapons and contraband in the 100 GHz to 1 THz region," IEEE Trans. Antennas Propag. **55**(11), 2944–2956 (2007).
7. J. Federici and L. Moeller, "Review of terahertz and subterahertz wireless communications," J. Appl. Phys. **107**(11), 111101 (2010).

Optics EXPRESS

8. D. J. Paul, "The progress towards terahertz quantum cascade lasers on silicon substrates," Laser Photonics Rev. **4**(5), 610–632 (2010).
9. S. Dhillon, M. Vitiello, E. Linfield, A. Davies, M. Hoffmann, J. Booske, C. Paoloni, M. Gensch, P. Weightman, G. Williams, E. Castro-Camus, D. Cumming, F. Simoens, I. Escorcia Carranza, J. Grant, S. Lucyszyn, M. Kuwata-Gonokami, K. Konishi, M. Koch, and M. Johnston, "The 2017 terahertz science and technology roadmap," J. Phys. D: Appl. Phys. **50**(4), 043001 (2017).
10. J. Faist, F. Capasso, D. L. Sivco, C. Sirtori, A. L. Hutchinson, and A. Y. Cho, "Quantum cascade laser," Science **264**(5158), 553–556 (1994).
11. R. Kohler, A. Tredicucci, F. Beltram, H. E. Beere, E. H. Linfield, A. G. Davies, D. A. Ritchie, R. C. Iotti, and F. Rossi, "Terahertz semiconductor-heterostructure laser," Nature **417**(6885), 156–159 (2002).
12. M. S. Vitiello, G. Scalari, B. Williams, and P. D. Natale, "Quantum cascade lasers: 20 years of challenges," Opt. Express **23**(4), 5167–5182 (2015).
13. L. Li, L. Chen, J. Zhu, J. Freeman, P. Dean, A. Valavanis, A. G. Davies, and E. H. Linfield, "Terahertz quantum cascade lasers with >1 W output powers," Electron. Lett. **50**(4), 309–311 (2014).
14. A. Wade, G. Fedorov, D. Smirnov, S. Kumar, B. S. Williams, Q. Hu, and J. L. Reno, "Magnetic-field-assisted terahertz quantum cascade laser operating up to 225 K," Nat. Photonics **3**(1), 41–45 (2009).
15. L. Bosco, M. Franckie, G. Scalari, M. Beck, A. Wacker, and J. Faist, "Thermoelectrically cooled THz quantum cascade laser operating up to 210 K," Appl. Phys. Lett. **115**(1), 010601 (2019).
16. P. Murzyn, C. R. Pidgeon, J.-P. R. Wells, I. V. Bradley, Z. Ikonic, R. W. Kelsall, P. Harrison, S. A. Lynch, D. J. Paul, D. D. Arnone, D. J. Robbins, D. Norris, and A. G. Cullis, "Picosecond intersubband dynamics in p-Si/SiGe quantum-well emitter structures," Appl. Phys. Lett. **80**(8), 1456–1458 (2002).
17. C. R. Pidgeon, P. J. Phillips, D. Carder, B. N. Murdin, T. Fromherz, D. J. Paul, W.-X. Ni, and M. Zhao, "Pump-probe measurement of lifetime engineering in SiGe quantum wells below the optical phonon energy," Semicond. Sci. Technol. **20**(10), L50–L52 (2005).
18. R. W. Kelsall, Z. Ikonic, P. Murzyn, C. R. Pidgeon, P. J. Phillips, D. Carder, P. Harrison, S. A. Lynch, P. Townsend, D. J. Paul, S. L. Liew, D. J. Norris, and A. G. Cullis, "Intersubband lifetimes in p – Si/SiGe terahertz quantum cascade heterostructures," Phys. Rev. B **71**(11), 115326 (2005).
19. M. Califano, N. Q. Vinh, P. J. Phillips, Z. Ikonić, R. W. Kelsall, P. Harrison, C. R. Pidgeon, B. N. Murdin, D. J. Paul, P. Townsend, J. Zhang, I. M. Ross, and A. G. Cullis, "Interwell relaxation times in p – Si/SiGe asymmetric quantum well structures: Role of interface roughness," Phys. Rev. B **75**(4), 045338 (2007).
20. M. Virgilio, M. Ortolani, M. Teich, S. Winnerl, M. Helm, D. Sabbagh, G. Capellini, and M. De Seta, "Combined effect of electron and lattice temperatures on the long intersubband relaxation times of Ge/Si_xGe_{1-x} quantum wells," Phys. Rev. B **89**(4), 045311 (2014).
21. D. Sabbagh, J. Schmidt, S. Winnerl, M. Helm, L. Di Gaspare, M. De Seta, M. Virgilio, and M. Ortolani, "Electron dynamics in silicon–germanium terahertz quantum fountain structures," ACS Photonics **3**(3), 403–414 (2016).
22. S. A. Lynch, D. J. Paul, R. Bates, Z. Ikonic, R. W. Kelsall, P. Harrison, D. J. Norris, A. G. Cullis, D. D. Arnone, C. R. Pidgeon, P. Murzyn, and A. Loudon, "THz electroluminescence from shallow level impurities in Si/SiGe heterostructures," in *Summaries of Papers Presented at the Lasers and Electro-Optics*. CLEO '02. Technical Digest p. 629 (2002).
23. S. A. Lynch, P. Townsend, G. Matmon, D. J. Paul, M. Bain, H. S. Gamble, J. Zhang, Z. Ikonic, R. W. Kelsall, and P. Harrison, "Temperature dependence of terahertz optical transitions from boron and phosphorus dopant impurities in silicon," Appl. Phys. Lett. **87**(10), 101114 (2005).
24. S. A. Lynch, R. Bates, D. J. Paul, D. J. Norris, A. G. Cullis, Z. Ikonic, R. W. Kelsall, P. Harrison, D. D. Arnone, and C. R. Pidgeon, "Intersubband electroluminescence from Si/SiGe cascade emitters at terahertz frequencies," Appl. Phys. Lett. **81**(9), 1543–1545 (2002).
25. R. Bates, S. A. Lynch, D. J. Paul, Z. Ikonic, R. W. Kelsall, P. Harrison, S. L. Liew, D. J. Norris, A. G. Cullis, W. R. Tribe, and D. D. Arnone, "Interwell intersubband electroluminescence from Si/SiGe quantum cascade emitters," Appl. Phys. Lett. **83**(20), 4092–4094 (2003).
26. P. Townsend, D. J. Paul, S. Lynch, R. Kelsall, Z. Ikonic, P. Harrison, D. J. Norris, G. Cullis, J. Zhang, X. Li, C. R. Pidgeon, B. Murdin, and P. Murzyn, "LO phonon scattering as a depopulation mechanism in Si/SiGe quantum cascades," in *IEEE 2nd International Conference on Group IV Photonics, 2005*. pp. 7–9 (2005).
27. G. Matmon, D. J. Paul, L. Lever, M. Califano, Z. Ikonić, R. W. Kelsall, J. Zhang, D. Chrastina, G. Isella, H. von Känel, E. Müller, and A. Neels, "Si/SiGe quantum cascade superlattice designs for terahertz emission," J. Appl. Phys. **107**(5), 053109 (2010).
28. K. Driscoll and R. Paiella, "Silicon-based injection lasers using electronic intersubband transitions in the L valleys," Appl. Phys. Lett. **89**(19), 191110 (2006).
29. M. D. Seta, G. Capellini, M. Ortolani, M. Virgilio, G. Grosso, G. Nicotra, and P. Zaumseil, "Narrow intersubband transitions in n-type Ge/SiGe multi-quantum wells: control of the terahertz absorption energy trough the temperature dependent depolarization shift," Nanotechnology **23**(46), 465708 (2012).
30. M. Virgilio, D. Sabbagh, M. Ortolani, L. Di Gaspare, G. Capellini, and M. De Seta, "Physical mechanisms of intersubband-absorption linewidth broadening in s-Ge/SiGe quantum wells," Phys. Rev. B **90**(15), 155420 (2014).

Optics EXPRESS

31. C. Ciano, M. Virgilio, M. Montanari, L. Persichetti, L. Di Gaspare, M. Ortolani, L. Baldassarre, M. H. Zoellner, O. Skibitzki, G. Scalari, J. Faist, D. J. Paul, M. Scuderi, G. Nicotra, T. Grange, S. Birner, G. Capellini, and M. De Seta, "Control of electron-state coupling in asymmetric Ge/Si-Ge quantum wells," Phys. Rev. Appl. **11**(1), 014003 (2019).
32. T. Grange, D. Stark, G. Scalari, J. Faist, L. Persichetti, L. Di Gaspare, M. De Seta, M. Ortolani, D. J. Paul, G. Capellini, S. Birner, and M. Virgilio, "Room temperature operation of n-type Ge/SiGe terahertz quantum cascade lasers predicted by non-equilibrium Green's functions," Appl. Phys. Lett. **114**(11), 111102 (2019).
33. T. V. Dinh, A. Valavanis, L. J. M. Lever, Z. Ikonić, and R. W. Kelsall, "Extended density-matrix model applied to silicon-based terahertz quantum cascade lasers," Phys. Rev. B **85**(23), 235427 (2012).
34. S. A. Lynch, D. J. Paul, P. Townsend, G. Matmon, Z. Suet, R. W. Kelsall, Z. Ikonic, P. Harrison, J. Zhang, D. J. Norris, A. G. Cullis, C. R. Pidgeon, P. Murzyn, B. Murdin, M. Bain, H. S. Gamble, M. Zhao, and W.-X. Ni, "Toward silicon-based lasers for terahertz sources," IEEE J. Sel. Top. Quantum Electron. **12**(6), 1570–1578 (2006).
35. A. De Rossi, M. Carras, and D. J. Paul, "Low-loss surface-mode waveguides for terahertz Si/SiGe quantum cascade lasers," IEEE J. Quantum Electron. **42**(12), 1233–1238 (2006).
36. L. Lever, A. Valavanis, C. A. Evans, Z. Ikonić, and R. W. Kelsall, "The importance of electron temperature in silicon-based terahertz quantum cascade lasers," Appl. Phys. Lett. **95**(13), 131103 (2009).
37. S. Fathololoumi, E. Dupont, C. Chan, Z. Wasilewski, S. Laframboise, D. Ban, A. Mátyás, C. Jirauschek, Q. Hu, and H. C. Liu, "Terahertz quantum cascade lasers operating up to ~ 200 K with optimized oscillator strength and improved injection tunneling," Opt. Express **20**(4), 3866–3876 (2012).
38. Y. J. Han, L. H. Li, J. Zhu, A. Valavanis, J. R. Freeman, L. Chen, M. Rosamond, P. Dean, A. G. Davies, and E. H. Linfield, "Silver-based surface plasmon waveguide for terahertz quantum cascade lasers," Opt. Express **26**(4), 3814–3827 (2018).
39. D. J. Fisher, *Diffusion in Silicon: 10 Years of Research* (Scitec Publications, 1998).
40. Y. Panayiotatos, R. V. Vovk, and A. Chroneos, "Gold and silver diffusion in germanium: a thermodynamic approach," J. Mater. Sci.: Mater. Electron. **28**(2), 1966–1970 (2017).
41. J. D. McBrayer, R. M. Swanson, and T. W. Sigmon, "Diffusion of metals in silicon dioxide," J. Electrochem. Soc. **133**(6), 1242–1246 (1986).
42. K. Gallacher, P. Velha, D. J. Paul, I. MacLaren, M. Myronov, and D. R. Leadley, "Ohmic contacts to n-type germanium with low specific contact resistivity," Appl. Phys. Lett. **100**(2), 022113 (2012).
43. D. C. S. Dumas, K. Gallacher, R. Millar, I. MacLaren, M. Myronov, D. R. Leadley, and D. J. Paul, "Silver antimony Ohmic contacts to moderately doped n-type germanium," Appl. Phys. Lett. **104**(16), 162101 (2014).
44. C. F. Klinghorn, *Semiconductor Optics* (Springer, 2012), 4th ed.
45. M. A. Ordal, R. J. Bell, R. W. Alexander, L. L. Long, and M. R. Querry, "Optical properties of fourteen metals in the infrared and far infrared: Al, Co, Cu, Au, Fe, Pb, Mo, Ni, Pd, Pt, Ag, Ti, V, and W," Appl. Opt. **24**(24), 4493–4499 (1985).
46. P. B. Johnson and R. W. Christy, "Optical constants of the noble metals," Phys. Rev. B **6**(12), 4370–4379 (1972).
47. R. L. Olmon, B. Slovick, T. W. Johnson, D. Shelton, S.-H. Oh, G. D. Boreman, and M. B. Raschke, "Optical dielectric function of gold," Phys. Rev. B **86**(23), 235147 (2012).
48. C. Sirtori, C. Gmachl, F. Capasso, J. Faist, D. L. Sivco, A. L. Hutchinson, and A. Y. Cho, "Long-wavelength ($\lambda \approx$ 8–11.5 μm) semiconductor lasers with waveguides based on surface plasmons," Opt. Lett. **23**(17), 1366–1368 (1998).
49. J. Frigerio, A. Ballabio, G. Isella, E. Sakat, G. Pellegrini, P. Biagioni, M. Bollani, E. Napolitani, C. Manganelli, M. Virgilio, A. Grupp, M. P. Fischer, D. Brida, K. Gallacher, D. J. Paul, L. Baldassarre, P. Calvani, V. Giliberti, A. Nucara, and M. Ortolani, "Tunability of the dielectric function of heavily doped germanium thin films for mid-infrared plasmonics," Phys. Rev. B **94**(8), 085202 (2016).
50. K. Gallacher, U. Griskeviciute, I. MacGilp, R. W. Millar, and D. J. Paul, "Understanding the sidewall dependence of loss for Ge-on-Si waveguides in the mid-infrared," in *2019 IEEE 16th International Conference Group IV Photonics (GFP)* pp. 1–2 (2019).
51. D. B. Tanner and D. C. Larson, "Electrical resistivity of silver films," Phys. Rev. **166**(3), 652–655 (1968).
52. R. A. Matula, "Electrical resistivity of copper, gold, palladium and silver," J. Phys. Chem. Ref. Data **8**(4), 1147–1298 (1979).
53. P. D. Desai, H. M. James, and C. Y. Ho, "Electrical resistivity of aluminum and manganese," J. Phys. Chem. Ref. Data **13**(4), 1131–1172 (1984).
54. I. Nakamichi and T. Kino, "Deviations from Matthiessen's rule on the surface scattering in aluminum," J. Phys. Soc. Jpn. **49**(4), 1350–1357 (1980).